1 **Author fixed this file based on the PDF also attached. Insert words in blue and fix notes in**

2 **yellow.**

3 **Revision 7**

4

5 **The uppermost mantle section below a remnant proto-Philippine Sea island**

6 **arc: Insights from the peridotite fragments from the Daito Ridge**

7 Tomoaki Morishita[1,2,*], Ken-Ichiro Tani[3], Yusuke Soda[1,4], Akihiro Tamura[1],

8 Tomoyuki Mizukami[1], and Biswajit Ghosh[1,5]

9

10 [1] School of Natural System, College of Science and Engineering, Kanazawa

11 University, Kakuma, Kanazawa, Ishikawa 920-1192, Japan

12 [2] Lamont-Doherty Earth Observatory, Columbia University, Palisades, NY 10964,

13 USA

14 [3] National Museum of Nature and Science, 4-1-1, Amakubo, Tsukuba-shi, Ibaraki

15 305-0005, Japan

16 [4] Department of Geosciences, Osaka City University, Osaka 558–8585, Japan

17 [5] Department of Geology, University of Calcutta, 35 Ballygunge Circular Road,

18 Kolkata 700019, India

19

20 * E-mail: tomo_make_a_wish@icloud.com

21

22

23 **ABSTRACT**

24 The Amami Plateau, Daito Ridge, and Oki-Daito Ridge of the northwestern

1

25   Philippine Sea Plate are remnants of Mesozoic island arcs. We have newly

26   recovered samples of peridotite and peridotite-derived minerals from the Daito

27   Ridge. The peridotite samples are composed of serpentinized/altered olivines,

28   orthopyroxene porphyroclasts, small clinopyroxenes and spinels, indicating a

29   harzburgitic origin. Chondrite- and primitive mantle-normalized trace element

30   patterns for clinopyroxenes are characterized by a steep positive slope from middle

31   rare earth elements to heavy rare earth elements (HREEs) plus yttrium. The light

32   rare earth elements (LREEs) and Sr and Zr contents of clinopyroxenes vary in

33   abundance, and some crystals have high LREE/HREE ratios coupled with positive

34   Sr and Zr anomalies. These petrological and geochemical characteristics are not

35   consistent with the Daito peridotites being the residue of a single partial melting

36   event including melt extraction expected for mid-ocean ridge mantle. Instead, the

37   peridotite source must have been enriched with slab-derived components, which are

2

38 associated with arc-related magma. Thus, it is concluded that the studied peridotite

39 fragments belong to an exhumed mantle section of a remnant proto-Philippine Sea

40 island arc.

41 **Keywords:** Philippine Sea Plate, Daito Ridge, remnant arc, peridotite, slab-derived
42 components, melting model

43

INTRODUCTION

45   The Philippine Sea Oceanic Plate has a complex architecture comprising

46 several geotectonic domains, including three back-arc basins: the West Philippine

47 Basin, the Parece Vela Basin, and the Shikoku Basin (Lallemand 2016, Wu et al.

48 2016, and references therein). These back-arc basins, together with the

49 Izu-Bonin-Mariana (IBM) Arc system, were formed following the initiation of

50 subduction of the Pacific Plate under the Philippine Sea Plate at ~ 52 Ma (Ishizuka

51 et al. 2011). Although the IBM Arc is one of the most studied intra-oceanic arcs,

52   little is known about the proto-Philippine Sea Plate that existed along the Pacific

53   Plate margin.

54   Cretaceous rocks have been reported in WNW-ESE trending sub-parallel

55   ridges (the Amami Plateau, the Daito Ridge, and the Oki-Daito Ridge and Plateau;

56   herein referred to collectively as the Daito Ridges) that line up from the north to

57   south across the northwestern Philippine Sea Plate (Hickey-Vergas 2005; Ishizuka et

58   al. 2011) (Fig. 1). Geophysical data indicate a total crustal thickness of 15-25 km in

59   the Daito Ridge area (Nishizawa et al. 2014), making it an ideal location to

60   reconstruct the tectonic evolution of the proto-Philippine Sea Plate.

61   Serpentinites and their minerals, such as chromian spinel and

62   clinopyroxene, have been recovered from the Daito Ridge in the past (Site 445 in

63   Fig. 1) (Yuasa and Watanabe 1977; Tokuyama et al., 1980), but their origin has

64   remained unclear. To further explore the architecture of the proto-Philippine Sea

4

65   Plate, we conducted sampling and direct observations of the Daito Ridges region

66   during two expeditions operated by the Japan Agency for Marine-Earth Science and

67   Technology (JAMSTEC). The first expedition (YK10-04) of the R/V YOKOSUKA

68   used a manned-submersible (SHINKAI 6500) coupled with a deep-tow camera

69   survey, and the second expedition (KR13-15) used a remotely operated vehicle

70   (KAIKO 66 7000II). An exposed deep-crustal section of gabbroic, granitic, and

71   metamorphic rocks was discovered, along with volcanic rocks ranging from basaltic

72   to andesitic in composition. These findings are consistent with the proposed arc

73   origin of the Daito Ridge region (Tokuyama, 1995; Hickey-Vargas, 2005; Ishizuka

74   et al., 2011). Geochemical and age data for igneous and metamorphic rock samples

75   collected from the ridge will be reported in a separate communication. Samples of

76   serpentinite were recovered from the Daito Ridge (location 7K611 in Fig. 1) during

77   the KR13-15 cruise. In this paper, we focus on these newly recovered samples and

5

78   discuss their origin in the context of the tectonic evolution of the Philippine Sea

79   Plate.

GEOLOGICAL BACKGROUND AND SAMPLE DESCRIPTIONS

81   The Philippine Sea Plate has a lozenge shape, with dimensions of ~3400

82   km from north to south and ~ 2600 km from east to west. Previous studies have

83   shown that it has experienced a complex tectonic evolution (e.g., Uyeda and Ben

84   Avraham 1972; Hilde and Lee 1984; Seno and Maruyama 1984; Hickey-Vargas

85   1991; Hall et al. 1995; Okino et al. 1999; Lallemand 2016; Wu et al. 2016). To the

86   northwest, the Philippine Sea Plate is subducting below the Eurasian Plate along the

87   Ryukyu Trench, up to the Nankai Trough. To the east, the Pacific Plate is subducting

88   below the Philippine Sea Plate, resulting in the formation of the IBM Arc. In the

89   southern part of the Philippine Sea Plate, a small divergent segment, the Ayu Trough,

90   is present. In addition, the plate hosts two back arc basins: the Eastern Shikoku and

91   Parece Vela basins, which opened during the Neogene (Karig 1971; Uyeda and Ben

92   Avraham 1972). The Daito Ridges itself has been interpreted as a remnant

93   Cretaceous-age segment of an island arc (Tokuyama 1995; Hickey-Vargas 2005;

94   Ishizuka et al. 2011).

95   Shiki et al. (1977) summarized the results of early 1970s cruise

96   expeditions to the northwestern Philippine Sea, and documented arc-type igneous

97   rocks and metamorphic schists (up to epidote-amphibolite facies) in the Daito Ridge

98   region, which they attributed to pre-Cenozoic island-arc activitiy. Yuasa and

99   Watanabe (1977) reported serpentinites, hornblende schist, and tremolite schist from

100   the Daito Ridge area, with the serpentinites consisting of mesh-structure serpentine,

101   green spinel, and magnetite, with small amounts of clinopyroxene. Tokuyama et al.

102   (1980) reported detrital minerals such as chromian spinel, diopside, and enstatite at

103   DSDP Site 445 (Daito Ridge), which were likely derived from serpentinized

7

104 peridotites.

105 The samples of the present study are characterized by peridotitic clasts

106 and the peridotite-derived minerals, such as orthopyroxene, spinel, and

107 clinopyroxene, cemented in a matrix consisting predominantly of carbonate

108 minerals (Fig. 2; Supplementary Appendix Fig A1.). Although the peridotitic

109 fragments are typically highly serpentinized/altered to dark brown-colored minerals,

110 they still contain fresh crystals of orthopyroxene, clinopyroxene, and spinel (Fig. 2).

111 Tremolite is locally associated with the orthopyroxene.

112 **MINERAL CHEMISTRY**

113 **Analytical Methods**

114 Major-element compositions of minerals (Tables 1-3 and Tables S1-S3 in

115 the Supplementary material) were determined using an electron probe

116 micro-analyzer (EPMA, JEOL JXA-8800 Superprobe) at Kanazawa University,

117   Japan. The analyses were performed with an accelerating voltage of 15 kV and a

118   beam current of 20 nA, using a 3 μm beam diameter. Natural and synthetic mineral

119   standards were used for calibration, and JEOL software using ZAF corrections was

120   employed for data reduction. In-house mineral standards (olivine, chromian spinel,

121   diopside, and K-feldspar) were measured repeatedly to monitor data quality. The

122   measured concentrations in these minerals were consistent with the averaged values

123   from long-term analyses, being within one standard deviation for every element.

124   Data precision, which was established through multiple analyses of one point in the

125   house-prepared standard minerals, was better than 5% and 10 % relative standard

126   deviation from the averaged values for elements with abundances of   > 0.5 wt. %

127   and < 0.5 wt. %, respectively. Details of the EPMA analyses can be found in

128   Morishita et al. (2003).

129   Rare earth element (REE) and trace element (Li, Ti, Sr, Y, Zr, and Nb)

9

130   compositions of orthopyroxene and clinopyroxene were determined using 193 nm

131   ArF excimer laser ablation-inductively coupled plasma-mass spectrometry

132   (LA-ICP-MS) at Kanazawa University (Agilent 7500S equipped with MicroLas

133   GeoLas Q-plus; Ishida et al. 2004). Clinopyroxenes and orthopyroxenes were

134   analyzed by ablating 50-90 μm and > 90 μm spot diameters, respectively, at 8 Hz.

135   The NIST SRM 612 standard was used as the primary calibration standard and was

136   analyzed at the beginning of each batch consisting of n ≤ 8 unknowns, with a linear

137   drift correction applied between each calibration. The element concentrations of

138   NIST SRM 612 for the calibration were selected from the preferred values of Pearce

139   et al. (1997). Data reduction was facilitated using ^{29}Si as an internal standard, based

140   on Si contents obtained by EPMA following the protocol essentially identical to that

141   outlined by Longerich et al. (1996). NIST SRM 614 was analyzed for quality

142   control during measurement. The measured concentrations in NIST SRM 614 glass,

143   which is a synthetic silicate glass with a nominal concentration of 1 ppm for 61

144   elements including REEs, were consistent with previously reported values to within

145   10 % relative standard deviation, and the data precision was better than 10 %

146   relative standard deviation for all the analyzed elements. Details of the analytical

147   method and data quality control are given by Morishita et al. (2005a, b).

148   Representative trace-element compositions of clinopyroxenes and orthopyroxenes

149   in the studied samples are listed in Table 3.

150   **Results**

151   The Cr# (= Cr/(Cr + Al) atomic ratio), Mg# (= Mg/(Mg + Fe^{2+}) atomic

152   ratio), and YFe^{3+} (= 100 Fe^{3+}/(Cr + Al + Fe^{3+}) atomic ratio) values of spinel in the

153   studied samples are 0.37-0.52, 0.56-0.68 and < 2.2, respectively (Fig. 3). The TiO_2

154   content of spinel is commonly below the detection limit (< 0.05 wt. %).

155   The Mg# (= Mg/(Mg + Fe^{total}) atomic ratio), Al_2O_3, and TiO_2 content of

11

156   orthopyroxene are 0.91-0.92, 2.0-2.6 wt.%, and < 0.05 wt.%, respectively.

157   Chondrite-normalized REE patterns for orthopyroxenes show an abrupt decrease

158   from heavy REEs (HREEs) to middle REEs (MREEs) (Fig. 4a). Middle and light

159   REEs (LREEs) are generally below the detection limit. Some of the clinopyroxenes

160   exhibit positive Zr and Sr anomalies (Fig. 4b).

161   The Mg# and Al_2O_3 content of clinopyroxene are 0.94-0.95 and 1.0-2.6

162   wt.%, respectively. The TiO_2 and Na_2O contents of clinopyroxene are low, at < 0.05

163   and < 0.1 wt.% respectively. Chondrite-normalized REE patterns for clinopyroxenes

164   show an abrupt decrease from HREEs to MREEs, and MREEs are generally below

165   the detection limit (Fig. 4a). Clinopyroxene shows variations in LREEs, Sr and Zr

166   concentrations. Some of the clinopyroxenes exhibit high LREE/HREE ratios

167   coupled with low abundances of MREEs (lower than the detection limit), resulting

168   in roughly V-shaped REE patterns and are Zr and Sr positive anomalies (Fig. 4b).

12

169   The partition coefficients of HREEs and Y between clinopyroxene and

170   orthopyroxene are consistent with those in earlier studies (Table S4 in the

171   Supplementary Material) (Ozawa and Shimizu 1995; Kelemen et al. 2003; McDade

172   et al. 2003a, b), indicating chemical equilibrium with regard to these elements.

173   **DISCUSSION**

174   **Protolith of the studied peridotite fragments**

175   The protolith of the studied peridotite fragments prior to

176   serpentinization/alteration was harzburgitic, as evident from the presence of

177   coarse-grained orthopyroxene porphyroclasts with minor amounts of clinopyroxene

178   and spinel, together with the serpentinized/altered olivines, as the dominant

179   minerals. Another line of evidence supporting a pre-serpentinization harzburgite

180   lithology is the reasonably high Cr # of the spinel in each sample (Fig. 3b). Major

181   element compositions of the Daito peridotite minerals overlap with those from

13

182 abyssal peridotites recovered from the mid-ocean ridges and fore-arc settings (Figs.

183 3 and 5). Therefore, it is not possible to use major element compositions of minerals

184 to constrain the tectonic setting from which the studied samples originated.

185 However, the trace element compositions of clinopyroxene does yield information

186 regarding the tectonic setting and/or magmatic processes experienced by the studied

187 samples, as explained below.

188 **Comparison with other peridotites**

189   Figure 6 compares the trace element compositions of clinopyroxenes in

190 the studied samples with that of other spinel peridotite samples analyzed in previous

191 studies. Geochemical data from peridotites with plagioclase and/or gabbroic veins

192 in previous works are not included for further discussions because

193 plagioclase-bearing (and/or gabbroic vein-bearing) peridotites undergo significantly

194 chemical alteration when they interact with melts during the formation of

14

195   plagioclases/gabbroic veins (e.g., Ohara, 2006).

196   The Daito clinopyroxenes are characterized by higher LREE/HREE ratios

197   and Sr contents than those of back-arc peridotites from the Philippine Sea Plate

198   (Ohara et al., 2002, 2003). The Zr and Sr are enriched relative to elements with

199   similar compatibility in some Daito clinopyroxenes (Fig. 4b). Figure 7 compares the

200   primitive-mantle-normalized Sr/Yb and Zr/Yb ratios in the Daito clinopyroxenes

201   with those of peridotite samples analyzed in other studies. The Yb content of

202   clinopyroxene in residual peridotites is a good indicator of the degree of partial

203   melting (e.g., Hellebrand et al., 2001). The Sr/Yb and Zr/Yb ratios decrease as the

204   degree of simple partial melting (e.g., fractional melting) increases. Clinopyroxenes

205   from the Izu-Bonin-Mariana fore-arc peridotites (Parkinson and Pearce 1998) and

206   the Hess Deep (Dick and Natland 1996) do not exhibit Zr enrichment, with the

207   exception of one sample from the Hess Deep that has geochemical characteristics

208   similar to those of the Daito clinopyroxenes (Figs. 6 and 7). Elevated Sr and Zr

209   concentrations are also observed in some Josephine Ophiolite peridotite samples,

210   which are thought to represent residual mantle after flux melting in a subduction

211   zone (e.g., Le Roux et al., 2014; Figs. 6 and 7).

212   **Magmatic processes deduced from geochemical modeling**

213   Here we discuss the magmatic processes that the samples are inferred to

214   have undergone, based on geochemical modeling using the trace element

215   compositions of clinopyroxenes. The trace element compositions of clinopyroxenes,

216   in terms of LREE/HREE ratios and Sr content, are distinct from the residue after a

217   single episode of fractional melting and melt extraction (Figs. 7 and 8), when

218   compared with typical residual peridotites that formed by decompression melting

219   (e.g., at a mid-ocean ridge). In addition, the positive Zr spike in clinopyroxene is a

220   unique characteristic of the studied samples (Figs. 5b and 7).

16

221   We modeled the clinopyroxene trace element patterns using 1) an

222   open-system melting model, in which the input and output of fluids/melts are

223   associated with partial melting and melt extraction of the peridotite itself (Ozawa

224   and Shimizu, 1995; Ozawa, 2001); and 2) a simplified plate model, in which porous

225   fluid/melt flow through mantle rocks is simulated by fluid/melt transfer from one

226   cell to another (e.g., Akizawa et al. (2016) after Varnières et al. (1997)). The melting

227   conditions and parameters used in the models are summarized in Table 4.

228   First, we estimated the flux composition using the open-system melting

229   model formulated by Ozawa (2001). As shown below, several parameters in the

230   melting model were adjusted to obtain the best possible results. To meet the

231   requirement of a steep gradient in REE distribution from MREEs to HREEs plus Y

232   (compare Fig. 8a and 8b), we assumed that the starting composition was a residue

233   following 5 % fractional melting of a depleted MORB mantle (DMM) (Workman

17

234   and Hart 2005) under pressure-temperature conditions of the garnet peridotite

235   stability field (first-stage melting). Melting proportions for the garnet peridotite are

236   as follows: 0.045 olivine + 0.965 clinopyroxene + 0.14 garnet = 0.14 orthopyroxene

237   + 1 melt (simplified after Walter, 1998). Then, the mineral mode for the garnet

238   stability conditions was converted to spinel peridotite based on the following

239   reaction: 3 orthopyroxene + 1 clinopyroxene + 1 spinel = 4 garnet + 1 olivine

240   (Takazawa et al. 1996). A total of 13 % melting was used for the second-stage

241   melting (flux-induced open system melting). Melting proportions for the

242   second-stage open system melting are as follows: 1 melt = 0.05 spinel + 0.45

243   orthopyroxene + 0.75 clinopyroxene − 0.25 olivine (simplified after Kinzler and

244   Grove, 1992). Influx composition with regard to La, Ce, Sr and Zr concentrations

245   was manipulated to match the analytically obtained values, assuming open-system

246   melting under the following conditions: 1) the presence of a critical melt fraction in

18

247   the system, at which the system becomes open to melt separation at a constant rate

248   of α=0.05; and 2) a dimensionless influx rate (influxed mass fraction of the initial

249   solid, divided by the degree of melting) of β = 1. The effect of trapped melt

250   crystallization was not considered. In contrast, influx compositions for HREEs plus

251   Y and Ti were assumed to be 0.002 times (except for Sm = 0.005 times) the

252   primitive mantle values. The calculated influx composition is characterized by high

253   LREE/HREE ratios, with positive Sr and Zr spikes (Fig. 8c). Of note, positive Zr

254   spikes are associated with boninites (Cameron et al. 1983; Bloomer et al. 1987;

255   Taylor et al. 1994; Li et al. 2013). Li et al. (2013) inferred a slab origin (via flux

256   melting) for boninites exhibiting a positive Zr spike from the Izu-Bonin-Mariana

257   Arc.

258   We have also estimated the composition of clinopyroxene composition by

259   modeling the second-stage open-system melting of the residual peridotites

19

260 following first-stage melting under the conditions stated above. We used the flux

261 composition of Li et al. (2013), which was estimated for slab-derived melts. The

262 conditions used for influx melting were as follows: degree of partial melting = 13 %,

263 $\alpha = 0.02$ and $\beta = 0.02$. Our calculation suggests that the observed positive Zr spike

264 in clinopyroxenes could be qualitatively reproduced by interaction with a

265 Zr-enriched slab-derived influx component under reasonable melting parameters.

266 However, the steep MREE-HREE gradient could not be accurately reproduced (Fig.

267 8d).

268 The clinopyroxenes (and orthopyroxenes) observed in thin sections show

269 a wide range of trace element compositions. Clinopyroxenes in a single thin section

270 might be derived from several peridotite samples because the studied samples are

271 aggregates of small peridotite fragments (Fig. 2). Although the special distribution

272 of the samples is not clear, this small-scale variation could be explained by the

20

273   percolation of fluids/melts through the peridotites. We tested this theory by applying

274   the plate model (Akizawa et al. 2016, simplified from Varnières et al. 1997:) to

275   simulate the chemical characteristics of the Daito clinopyroxenes. The chemical

276   compositions of percolating melt changes with increasing cell numbers, j, of the

277   percolation column, according to the following equation: $C_{melt\,j} = (C_{melt\,(j-1)} + \alpha_j C_{cpx}$

278     $_0)/(1 + D\alpha_j)$. The initial trace element composition of the percolating melt ($C_{melt\,0}$)

279   and initial clinopyroxene ($C_{cpx\,0}$) are the same as those used in the open-system

280   melting model (taken from Li et al., 2013). The residue after 13 % fractional

281   melting under conditions of the stability of spinel peridotite is assumed to be formed

282   from a residual following 5 % fractional melting under the stability conditions of

283   garnet peridotite (Fig. 8b). We assume that the percolating melt/fluid mass ratio

284   decreases gradually away from the location where the melt-rock reaction was

285   initiated. The clinopyroxene/melt mass ratio (αj) is assumed to change from $\alpha_1 = 1$

21

286   to $\alpha_j = 2 \times (j - 1)$ $(j > 1)$. Positive Sr and Zr anomalies in clinopyroxenes are

287   observed in reacted columns that are located far from the first percolating column

288   (Figs. 8e and f).

289   In conclusion, both open-system melting and plate models with Sr- and

290   Zr-enriched fluids/melts, which considered representative of slab-derived melts, can

291   qualitatively reproduce the chemical characteristics of the Daito clinopyroxenes,

292   implying that the Daito peridotites were formed in an island arc environment. These

293   results support the theory that the Daito Ridge region represents a section of the

294   uppermost mantle to the lower crust from a remnant arc of the proto-Philippine Sea

295   Plate.

296   **IMPLICATIONS**

297   Newly recovered peridotite samples from the Daito Ridge are of subarc

298   origin. Our results, coupled with acquisition of granitic samples from the Daito

299 Ridges, suggest that the Daito Ridge represents an exposed mantle section of the

300 proto-Philippine Sea Plate. This raises the question of how the uppermost mantle

301 section of island arc was brought to the ocean floor without having been thrust there

302 during plate convergence, as occurs during ophiolite obduction. Further detailed

303 investigation of the studied samples, plus similar samples from ophiolites, is needed

304 to enhance our understanding of such mantle section and their exhumation.

305

306 **ACKNOWLEDGEMENTS**

23

312   Grants-in-Aid for Scientific Research from the Ministry of Education Culture,

313   Sports, Science and Technology of Japan, awarded to TM (Nos. 26287134 and

314   16H05741), and KT (No. 24684037).

315

24

316

317   **REFERENCES CITED**

318   Akizawa, N., Ozawa, K., Tamura, A., Michibayashi, K., and Arai, S. (2016)
319   Three-dimensional evolution of melting, heat and melt transfer in ascending
320   Mantle beneath a aast-spreading ridge segment constrained by trace elements in
321   clinopyroxene from concordant dunites and host harzburgites of the Oman
322   ophiolite. Journal of Petrology, 57, 777-814.

323   Bloomer, S.H., and Hawkins, J.W. (1987) Petrology and geochemistry of boninite
324   series volcanic rocks from the Mariana trench. Contributions to Mineralogy and
325   Petrology, 97, 361-377.

326   Cameron, W.E., McCulloch, M.T., and Walker, D.A. (1983) Boninite petrogenesis:
327   chemical and Nd-Sr isotopic constraints. Earth and Planetary Science Letters,
328   65, 75-89.

329   Dick, H.J.B., and Natland, J.H. (1996) Late-stage melt evolution and transport in the
330   shallow mantle beneath the East Pacific Rise. Proceedings of the Ocean
331   Drilling Program, 147 Scientific Results, 103-134.

332   Gaetani, G.A., and Grove, T.L. (1998) The influence of water on melting of mantle
333   peridotite. Contributions to Mineralogy and Petrology, 131, 323-346.

334   Hall, R., Ali, J.R., Anderson, C.D., and Baker, S.J. (1995) Origin and motion history
335   of the Philippine Sea Plate. Tectonophysics, 251, 229-250.

336   Hellebrand, E., Snow, J.E., Dick, H.J.B and Hofmann, A.W. (2001) Coupled major
337   and trace elements as indicators of the extent of melting in mid-ocean-ridge
338   peridotites. Nature, 410, 677-681.

339   Hickey-Vargas, R. (1991) Isotope characteristics of submarine lavas from the
340   Philippine Sea: implications for the origin of arc and basin magmas of the
341   Philippine tectonic plate. Earth and Planetary Science Letters, 107, 290–304.

25

342 Hickey-Vargas, R. (2005) Basalt and tonalite from the Amami Plateau, northern
343   West Philippine Basin: new early Cretaceous ages and geochemical results, and
344   their petrologic and tectonic implications. The Island Arc, 14, 653-665.

345 Hilde, T.W.C., and Lee, C.-S. (1984) Origin and evolution of the west Philippine
346   basin: a new interpretation. Tectonophysics, 102, 85-104.

347 Ishizuka, O., Taylor, R.N., Yuasa, M., and Ohara, Y. (2011) Making and breaking an
348   island arc: a new perspective from the Oligocene Kyushu-Palau arc, Philippine
349   Sea.   Geochemistry   Geophysics   Geosystems,
350   Q05005,doi:10.1029/2010GC003440.

351 Karig D.E. (1971) Origin and development of marginal basins in the western Pacific.
352   Journal of Geophysical Research, 76, 2542–2561.

353 Kelemen, P.B., Yogodzinski, G.M. and Scholl, D.W. (2003) Along-strike variation in
354   the Aleutian Island Arc: Genesis of high Mg# andesite and implications for
355   continental curst. Geophysical Monograph 138, 223-276.

356 Kinzler, R.J., and Grove, T.L. (1992) Primary magmas of mid-ocean ridge basalts 1.
357   Experiments and Methods. Journal of Geophysical Research, 97, 6885-6906.

358 Klein, G.dV., and Kobayashi, K. (1980) Geological summary of the north Philippine
359   Sea, based on Deep Sea Drilling Project Leg 58 results. Initial Reports of the
360   Deep Sea Drilling Project, 58, 951-961.

361 Lallemand, S. (2016) Philippine Sea Plate inception, evolution, and consumption
362   with special emphasis on the early stages of Izu-Bonin-Mariana subduction.
363   Progress in Earth and Planetary Science, 3, doi:10.1186/s40645-016-0085-6.

364 Le Roux, V., Dick, H.J.B., and Shimizu, N. (2014) Tracking flux melting and melt
365   percolation in supra-subduction peridotites (Josephine ophiolite, USA).
366   Contributions   to   Mineralogy   and   Petrology,   168,   1064,   doi:
367   10.1007/s00410-014-1064-9.

26

368   Li, Y.-B., Kimura, J.-I., Machida, S., Ishii, T., Ishiwatari, A., Maruyama, S., Qiu,
369   H.-N., Ishikawa, T., Kato, Y., Haraguchi, S., Takahashi, N., Hirahara, Y., and
370   Miyazaki, T. (2013) High-Mg Adakite and Low-Ca Boninite from a Bonin
371   Fore-arc Seamount: Implications for the Reaction between Slab Melts and
372   Depleted Mantle. Journal of Petrology, 54, 1149-1175.

373   Longerich, H.P., Jackson, S.E., and Günther, D. (1996) Laser ablation inductively
374   coupled plasma mass spectrometric transient signal data acquisition and analyte
375   concentration calculation. Journal of Analytical Atomic Spectrometry, 11,
376   899-904.

377   Loocke, M., Snow, J.E., and Ohara, Y. (2013) Melt stagnation in peridotites from
378   the Godzilla Megamullion Oceanic Core Complex, Parece Vela Basin,
379   Philippine Sea. Lithos, 182-183.

380   McDade, P., Blundy, J.D., and Wood, B.J. (2003a) Trace element partitioning on the
381   Tinaquillo Lherzoltie solidus at 1.5 GPa. Physics of the Earth and Planetary
382   Interiors, 139, 129-147.

383   McDade, P., Blundy, J.D., and Wood, B.J. (2003b) Trace element partitioning
384   between mantle wedge peridotite and hydrous MgO-rich melt. American
385   Mineralogist, 88, 1825-1831.

386   McDonough, W.F., and Sun, S.-s. (1995) The composition of the Earth. Chemical
387   Geology, 120, 223-253.

388   Morishita, T., Arai, S., and Tamura, A. (2003) Petrology of an apatite-rich layer in
389   the Finero phlogopite-peridotite, Italian Western Alps; implications for
390   evolution of a metasomatising agent. Lithos, 69, 37-49.

391   Morishita, T., Ishida, Y., and Arai, S. (2005a) Simultaneous determination of
392   multiple trace element compositions in thin (< 30 μm) layers of BCR-2G by
393   193 nm ArF excimer laser ablation-ICP-MS: implications for matrix effect and

394   element fractionation on quantitative analysis. Geochemical Journal, 39,
395   327-40.

396 Morishita, T., Ishida, Y., Arai, S., and Shirasaka, M. (2005b) Determination of
397   multiple trace element compositions in thin (< 30 μm) layers of NIST SRM 614
398   and 616 using laser ablation ICP-MS. Geostandard and Geoanalytical Research,
399   29, 107-122.

400 Morishita, T., Dilek, Y., Shallo, M., Tamura, A., and Arai, S. (2011) Insight into the
401   uppermost mantle section of a maturing arc: the Eastern Mirdita ophiolite
402   Albania. Lithos, 124, 215-226.

403 Morishita, T., Nakamura, K., Shibuya, T., Kumagai, H., Sato, T., Okino, K., Sato, H.,
404   Nauchi, R., Hara, K., and Takamaru, R. (2015) Petrology of peridotites and
405   related gabbroic rocks around the Kairei hydrothermal field in the Central
406   Indian Ridge, in Subseafloor Biosphere Linked to Hydrothermal Systems:
407   TAIGA Concept edited by Ishibashi, J., Okino, K. and Sunamura, M., Springer,
408   doi: 10.1007/ 978-4-431-54865-2_14.

409 Nishizawa, A., Kaneda, K., Katagiri, Y., and Oikawa, M. (2014) Wide-angle
410   refraction experiments in the Daito Ridges region at the northwestern end of the
411   Philippine Sea plate. Earth and Planetary Science, 66,
412   http://www.earth-planets-space.com/content/66/1/25.

413 Ohara, Y., Stern, R. J., Ishii, T., Yurimoto, H., and Yamazaki, T. (2002) Peridotites
414   from the Mariana Trough: First look at the mantle beneath an active backarc
415   basin. Contributions to Mineralogy and Petrology, 143, 1–18.

416 Ohara, Y., Fujioka, K., Ishii, T., and Yurimoto, H. (2003) Peridotites and gabbros
417   from the Parece Vela backarc basin: Unique tectonic window in an extinct
418   backarc spreading ridge. Geochemistry Geophysics Geosystems 4,
419   doi:10.1029/2002GC000469.

420   Okino, K., Ohara, Y., Kasuga, S., and Kato, Y. (1999) The Philippine Sea: A new
421   survey results reveal the structure and history of the marginal basins.
422   Geophysical Research Letter, 26, 2287–2290.

423   Ozawa, K. (2001) Mass balance equations for open magmatic systems: trace
424   element behavior and its application to open system melting in the upper mantle.
425   Journal of Geophysical Research, 106, 13407-13434.

426   Ozawa, K., and Shimizu, N. (1995) Open-system melting in the upper mantle:
427   constraints from the Hayachine-Miyamori ophiolite, northeastern Japan.
428   Journal of Geophysical Research, 100, 22315-22335.

429   Parkinson, I.J., and Pearce, J.A. (1998) Peridotites from the Izu-Bonin-Mariana
430   Forearc (ODP Leg125): Evidence for mantle melting and melt-mantle
431   interaction in a supra-subduction zone setting. Journal of Petrology, 39,
432   1577-1618.

433   Ryan, W. B. F., Carbotte, S. M., Coplan, J. O., O'Hara, S., Melkonian, A., Arko, R.,
434   Weissel, R.A., Ferrini, V., Goodwillie, A., Nitsche, F., Bonczkowski, J., and
435   Zemsky, R. (2009) Global multi-resolution topography synthesis. Geochemistry
436   Geophysics Geosystems. 10, Q03014.
437   http://dx.doi.org/10.1029/02008GC002332.

438   Seno, T., and Maruyama, S. (1984) Paleogeographic reconstruction and origin of the
439   Philippine Sea. Tectonophysics, 102, 53-84.

440   Shiki, T., Misawa, Y., Konda, I., and Nishimura, A. (1977) Geology and geohistory
441   of the Northwestern Philippine Sea, with special reference to the results of the
442   recent Japanese research cruises. Memoirs of the Faculty of Science, Kyoto
443   University, Series of geology and mineralogy, 44, 67-78.

444   Takazawa, E., Frey, F., Shimizu, N. and Obata, M. (1996) Evolution of the Horoman
445   Peridotite (Hokkaido, Japan): Implications from pyroxene compositions.

446   Chemical Geology, 134, 3-26.

447   Taylor, R.N., Nesbitt, R.W., Vidal, P., Harmon, R.S., Auvray, B., and Croudace, I.W.

448   (1994) Mineralogy, chemistry, and genesis of the Boninite series volcanics,

449   Chichijima, Bonin Islands, Japan. Journal of Petrology, 35, 577-617,

450   doi:10.1093/petrology/35.3.577.

451   Tokuyama, H. (1995) Origin and development of Philippine Sea. in Geology and

452   Geophysics of the Philippine Sea - Japan-Russia-China Monograph, edited by

453   Tokuyama, H. et al., Terra Scientific Publishing Company, 155-163.

454   Tokuyama, H., Yusa, M., and Mizuno, A. (1980) Conglomerate and sandstone

455   petrography, Deep Sea Drilling Project Site 445, Philippine Sea. Initial Reports

456   of the Deep Sea Drilling Project, 58, 629-641.

457   Uyeda, S., and Ben Avraham, Z. (1972) Origin and development of the Philippine

458   Sea, Nature, 40, 176–178.

459   Vernières, J., Godard, M., and Bodinier, J.-L. (1997) A plate model for the

460   simulation of trace element fractionation during partial melting and magma

461   transport in the Earth's upper mantle. Journal of Geophysical Research, 102,

462   24771–24784.

463   Walter, M.J. (1998) Melting of garnet peridotite and the origin of komatiite and

464   depleted lithosphere. Journal of Petrology, 39, 29-60.

465   Warren, J.M. (2016) Global variations in abyssal peridotite compositions. Lithos,

466   248-251, 193-219.

467   Workman, R.K., and Hart, S.R. (2005) Major and trace element compositions of the

468   depleted MORB mantle (DMM). Earth and Planetary Science Letters, 231,

469   53-72.

470   Wu, J., Suppe, J., Lu, R., and Kanda, R. (2016) Philippine Sea and East Asian plate

471   tectonics since 52Ma constrained by new subducted slab reconstruction

472   methods. Journal of Geophysical Research, 121, 4670–4741.

473   Yuasa, M., and Watanabe, T. (1977) Pre-Cenozoic metamorphic rocks from the

474   Daito ridge in the Northern Philippine Sea. The Journal of the Japanese

475   Association of Mineralogists, Petrologists and Economic Geologists, 72,

476   241-251.

477

478

31

479

480   FIGURE 1. (a) Bathymetric map of the Daito Ridge, prepared using GeoMapApp

481   (Ryan et al. 2009). (b) Enlargement of the area outlined in (a), showing the

482   sampling location (7K#611) of this study. The location of Site 445 of DSDP Leg 58

483   is also shown (Klein and Kobayashi 1980). Ayu T. = Ayu Trough, C.B.F. rift =

484   Central Basin Fault rift, L.O. FZ = Luzon-Okinawa Fracture Zone, Nankai T. =

485   Nankai Trough.

486

487   FIGURE 2. Typical examples of serpentinized clasts (brown-colored areas in the

488   image) plus peridotite-derived minerals, hosted in a carbonate matrix (transparent

489   areas). (a) Thin section of sample R08-1. (b) Photomicrograph (plane-polarized

490   light) of a lithic clast within sample R08-1, containing spinel, orhotpyroxene, and

491   clinopyroxene. (c) Same as in (b), but in cross-polarized light.

492

493   FIGURE 3. Relationship between the Mg# and Cr# of spinel. (a) Comparison with

494   the Philippine Sea back-arc peridotites. Data are from Loocke et al. (2013) and the

495   Dunite-type (D-type) peridotites of Ohara et al. (2003). (b) Comparison with typical

496   mid-ocean ridge and fore-arc peridotites. The compositional ranges for mid-ocean

497   ridge peridotites and fore-arc peridotites are compiled by Morishita et al. (2011),

498   and those for mid-ocean ridge lherzolites and harzburgites are from Warren (2016).

499

500   FIGURE   4.   (a)   Chondrite-normalized   REE   patterns   and   (b)

501   primitive-mantle-normalized trace element patterns of the Daito clinopyroxenes and

502   orthopyroxenes. Chondrite and primitive mantle values are from McDonough and

503   Sun (1995). The typical detection limit of elemental analyses is also shown for 50

504   μm (+) and 90 μm (X) diameter laser beams.

505

506   FIGURE 5. Relationship between the Al_2O_3 content (wt.%) in the cores of
507   orthopyroxene porphyroclasts and the Cr# in coexisting spinel. The compositional
508   ranges for mid-ocean ridge and fore-arc peridotites are from Morishita et al. (2015).
509

510   FIGURE 6. Comparisons between primitive-mantle-normalized trace element
511   patterns for clinopyroxenes in the studied samples (gray) and those from previous
512   studies (black). The primitive-mantle values are from McDonough and Sun (1995).
513   (a) Comparison with Philippine Sea back-arc peridotites, which have been modified
514   to a lesser extent by melt impregnation. Data are from Ohara et al. (2002), and the
515   fertile peridotites (F-type) studied by Ohara et al. (2003). (b) Comparison with
516   Izu-Bonin-Mariana fore-arc peridotites. Data are from Parkinson and Pearce (1998).
517   (c) Comparison with the mantle section of the Josephine Ophiolite, Oregon, USA.
518   Data are from Le Roux et al. (2014). The stippled lines represent samples that show
519   anomalous trends. (d) Comparison with peridotite samples from the Hess Deep of
520   the East Pacific Rise. One sample, depicted by the dotted line, displays a similar
521   trend to the Daito Ridge peridotites. Data are from Dick and Natland (1996).
522

523   FIGURE 7. Correlations between primitive-mantle-normalized Sr/Yb and Zr/Yb
524   ratios in clinopyroxenes from the Daito Ridge (this study), Izu-Bonin-Mariana
525   (IBM) fore-arc peridotites (Parkinson and Pearce, 1998), the Josephine Ophiolite
526   (Le Roux et al., 2014), and the Hess Deep (Dick and Natland, 1996). The primitive
527   mantle values are from McDonough and Sun (1995). The fractional melting trend is
528   also shown.
529

530   FIGURE 8. Observed and modeled primitive-mantle-normalized trace element

33

531   patterns for clinopyroxene (cpx). Details of how the data were obtained are outlined

532   in the text. (a) Modeled clinopyroxene trace element compositions after fractional

533   melting under conditions of the spinel (spl) peridotite stability field. (b) Modeled

534   clinopyroxene trace element compositions after fractional melting under conditions

535   of the spinel (spl) peridotite stability field, following previous fractional melting

536   under conditions of the garnet (grt) peridotite stability field. The patterns shown are

537   for residue after 5 %, 10 %, and 15 %, and 5%, 10% and 13 % fractional melting

538   from depleted MORB mantle (DMM) of Workman and Hart (2005). (c) Modeled

539   influx and clinopyroxene compositions after open-system melting. (d) Modeled

540   clinopyroxene compositions after influx melting under conditions of the spinel

541   peridotite stability field. The influx composition, taken from Li et al. (2013), is

542   estimated from slab-derived boninite melts from the Izu-Bonin-Mariana fore-arc. (e

543   and f) Modeled clinopyroxene compositions after simplified plate model. The initial

544   trace element compositions that we used for the percolating melt and initial

545   clinopyroxene are the same as those used in the open-system melting model (d). The

546   percolating melt mass ratio, (αj), decreases gradually from $\alpha_1 = 1$ to $\alpha_j = 2 \times (j - 1)$ (j

547   > 1) away from the location where the melt–rock reaction was initiated. The

548   patterns shown are for compositions after $\alpha1 - \alpha7$ plate models.

549

550   Table 1. Averaged spinel compositions

551

552   SD = 1 sigma standard deviation, Mg# = Mg/(Mg + Fe^{2+}), Cr# = Cr/(Cr + Al),

553   YFe^{3+} = Fe^{3+}/(Cr + Al + Fe^{3+}). Fe_2O_3 and FeO were calculated based on

554   stoichiometry.

555

556   Table 2. Representative orthopyroxene compositions

557

558   Anal# = analytical point number, Mg# = Mg/(Mg + Fe^{total}) atomic ratio, Cr# =

559   Cr/(Cr + Al) atomic ratio

560

561   Table 3. Representative clinopyroxene compositions

562

563   Anal# = analytical point number, Mg# = Mg/(Mg + Fe^{total}) atomic ratio, Cr# =

564   Cr/(Cr + Al) atomic ratio, LA dia = Laser diameter, < = lower than detection limit,

565   n.a. = not analyzed

566

567   Table 4. Melting conditions and parameters used for geochemical models

35

568

Table 1. Averaged spinel compositions

Sample	R01		R02		R03		R08-1	
wt%	spinel	SD (n = 7)	spinel	SD (n = 3)	spinel	SD (n = 6)	spinel	SD (n = 11)
TiO_2	< 0.05		< 0.05		< 0.05		< 0.05	0.01
Al_2O_3	33.73	2.7	30.32	2	32.14	1.4	29.96	1.7
Cr_2O_3	35.29	2.7	38.84	3.1	36.39	1.7	39.32	1.9
Fe_2O_3*	2.19	0.3	1.14	1.7	1.71	0.8	0.78	0.3
FeO	13.78	0.6	15.68	0.5	16.36	0.3	16.27	0.7
MnO	0.21	0.03	0.23	0.04	0.24	0.05	0.27	0.04
MgO	15.53	0.3	13.81	0.6	13.61	0.4	13.35	0.5
CaO	< 0.03		< 0.03		< 0.03		< 0.03	
NiO	0.11	0.02	0.11	0.04	0.1	0.03	0.08	0.03
Total	100.8		100.1		100.6		100	
Mg#	0.668	0.01	0.611	0.02	0.597	0.01	0.594	0.02
Cr#	0.413	0.04	0.462	0.04	0.432	0.02	0.468	0.03
YFe^{3+}	0.024	0.003	0.013	0.02	0.019	0.009	0.009	0.003

SD = 1 sigma standard deviation

Fe_2O_3 and FeO were calculated based on stoichiometry

Mg#=Mg/(Mg+Fe^{2+}); Cr#=Cr/(Cr+Al); YFe^{3+}=Fe^{3+}/(Cr+Al+Fe^{3+})

569

Table 2. Representative orthopyroxene compositions

Sample #	R01	R01	R02	R03	R03	R03	R08-1	R08-1
Anal #	1-67	1-68	2-135	2-101	3-102	3-125	1-44	1-10
SiO_2	57.27	57.27	57.02	57.24	56.81	56.24	57.41	56.28
TiO_2	< 0.05	< 0.05	< 0.05	< 0.05	< 0.05	< 0.05	< 0.05	< 0.05
Al_2O_3	2.46	2.43	2.51	2.17	2.40	2.55	2.21	2.34
Cr_2O_3	0.68	0.64	0.75	0.46	0.61	0.74	0.65	0.70
FeO	5.51	5.28	5.62	5.45	5.45	5.46	5.44	5.18
MnO	0.14	0.18	0.08	0.14	0.13	0.13	0.16	0.14
MgO	34.47	34.10	34.38	34.42	34.19	33.36	34.18	33.25
CaO	0.75	0.84	0.54	0.45	0.52	1.40	0.80	2.36

Na_2O	< 0.02	< 0.02	< 0.02	< 0.02	< 0.02	< 0.02	< 0.02	< 0.02
K_2O	< 0.02	< 0.02	< 0.02	< 0.02	< 0.02	< 0.02	< 0.02	< 0.02
NiO	< 0.05	0.08	< 0.05	0.11	0.06	0.11	0.08	0.09
total	101.3	100.8	100.9	100.4	100.2	100.0	100.9	100.4
Mg#	0.918	0.920	0.916	0.918	0.918	0.916	0.918	0.920
Cr#	0.155	0.149	0.166	0.125	0.145	0.163	0.165	0.168
LA#	#201	#203	#101			#Y111	#112	#111
ppm								
Ti	70.1	31.9	47.2	n.a.	n.a.	62.0	51.0	52.7
Sr	0.005	0.039	0.149	n.a.	n.a.	0.478	0.311	0.004
Y	0.115	0.09	0.092	n.a.	n.a.	0.124	0.089	0.082
Zr	0.034	0.079	0.062	n.a.	n.a.	0.526	0.271	0.031
Nb	0.040	0.041	0.040	n.a.	n.a.	0.073	0.027	0.029
Dy	0.01	0.005	0.005	n.a.	n.a.	0.009	0.006	0.004
Ho	0.003	0.003	0.002	n.a.	n.a.	0.006	0.003	0.003
Er	0.024	0.019	0.017	n.a.	n.a.	0.016	0.017	0.016
Tm	0.007	0.005	0.005	n.a.	n.a.	0.005	0.004	0.004
Yb	0.066	0.05	0.055	n.a.	n.a.	0.058	0.050	0.048
Lu	0.017	0.009	0.014	n.a.	n.a.	0.009	0.010	0.011

Anal # = analytical point number, Mg# = Mg/(Mg+Fe) atomic ratio, Cr# = Cr/(Cr + AL) atomic ratio, n.a. = not analyzed

570

571

Table 3. Representative clinopyroxene compositions

Sample #	R01	R01	R01	R01	R01	R01	R01	R01	R01	R02	R02	R03	R03	R03	R08	R08	R08
Anal #	2-69	1-75	2-76	2-78	1-79	2-81	1-86	2-91	1-95	4-137	3-142	2-99	2-105	1-115	1-23	1-25	1-51
wt %																	
SiO_2	53.10	53.91	53.39	53.95	53.84	53.37	54.05	53.40	53.48	53.86	53.97	54.06	53.61	53.90	54.33	53.45	53.28
TiO_2	< 0.05	0.05	< 0.05	< 0.05	< 0.05	< 0.05	< 0.05	< 0.05	< 0.05	< 0.05	< 0.05	< 0.05	< 0.05	< 0.05	< 0.05	< 0.05	< 0.05
Al_2O_3	2.69	1.70	2.89	1.62	2.77	2.10	1.70	2.50	2.55	2.10	2.21	2.33	2.12	2.21	2.06	1.98	2.24
Cr_2O_3	0.96	0.70	1.04	0.38	0.96	0.56	0.62	0.78	0.93	0.62	0.74	0.83	0.88	0.73	0.85	0.69	0.89
FeO	1.85	1.82	2.24	1.86	2.21	1.93	1.86	2.10	1.71	2.00	1.89	1.67	1.68	2.02	1.56	1.65	1.85
MnO	0.08	< 0.05	0.10	0.06	0.08	0.13	0.08	0.08	0.07	0.12	0.06	0.08	0.05	0.05	0.05	0.08	0.06

37

MgO	17.18	17.35	17.87	17.86	18.01	17.81	18.18	17.43	17.15	17.56	17.48	17.32	17.38	17.50	17.26	17.46	17.47
CaO	23.73	24.31	22.75	23.57	22.36	23.57	21.89	23.51	24.35	23.75	23.89	24.42	24.42	23.75	24.33	24.01	23.46
Na_2O	0.08	0.08	0.07	0.06	0.08	0.07	0.18	0.06	0.06	0.04	0.07	0.04	0.05	0.04	0.11	0.10	0.09
K_2O	< 0.02	< 0.02	< 0.02	< 0.02	< 0.02	< 0.02	< 0.02	< 0.02	< 0.02	< 0.02	< 0.02	< 0.02	< 0.02	< 0.02	< 0.02	< 0.02	< 0.02
NiO	< 0.05	< 0.05	< 0.05	< 0.05	< 0.05	< 0.05	< 0.05	0.05	0.05	0.05	< 0.05	0.05	0.05	0.06	< 0.05	0.05	< 0.05
total	99.7	100.0	100.4	99.4	100.3	99.6	98.6	99.9	100.4	100.1	100.3	100.8	100.3	100.3	100.6	99.5	99.4
Mg#	0.943	0.944	0.934	0.945	0.936	0.943	0.946	0.937	0.947	0.940	0.943	0.949	0.949	0.939	0.952	0.950	0.944
Cr#	0.193	0.215	0.195	0.135	0.189	0.152	0.198	0.174	0.197	0.166	0.183	0.193	0.218	0.181	0.216	0.189	0.210
ppm																	
LA dia (µm)	50	60	90	50	90	60	90	50	50			50	50	50	60	50	60
ppm																	
Li	5.2	6.9	7.5	5.6	5.4	5.7	6.7	6.0	4.0	n.a.	n.a.	2.8	2.4	3.1	4.2	5.3	5.7
Sc	45	54	52	51	51	53	56	54	57	n.a.	n.a.	60	61	50	50	55	48
Ti	58	66	61	130	82	78	79	68	103	n.a.	n.a.	57	64	47	121	139	90
V	139	143	150	155	153	133	126	148	166	n.a.	n.a.	164	176	159	178	173	165
Cr	6697	7277	7827	5902	7200	4737	6118	6661	8079	n.a.	n.a.	5354	6605	5330	6568	7229	7037
Co	22	19	23	25	23	21	17	23	20	n.a.	n.a.	18	18	22	20	19	20
Ni	396	337	389	368	393	349	353	399	356	n.a.	n.a.	332	324	384	347	358	370
Sr	0.21	0.55	1.40	0.17	0.10	0.33	0.70	0.20	0.76	n.a.	n.a.	0.10	0.02	0.37	0.13	0.31	0.24
Y	0.64	0.69	0.71	0.86	0.88	0.83	0.84	0.71	1.14	n.a.	n.a.	0.58	0.69	0.54	0.60	0.73	0.55
Zr	0.32	0.87	1.46	0.14	0.11	0.49	1.10	0.80	1.55	n.a.	n.a.	0.17	0.09	1.13	0.10	0.79	0.33
Nb	0.041	0.039	0.053	0.036	0.047	0.035	0.044	0.043	0.048	n.a.	n.a.	0.035	0.048	0.038	0.042	0.043	0.034
Ba	0.047	0.106	0.382	<	<	0.092	0.300	<	0.276	n.a.	n.a.	<	<	0.220	<	0.064	0.079
La	0.006	0.009	0.027	<	0.003	0.006	0.010	<	0.014	n.a.	n.a.	<	<	0.020	<	0.006	0.005
Ce	0.016	<	0.026	0.008	0.010	0.007	0.011	0.012	0.017	n.a.	n.a.	<	<	<	<	<	<
Pr	<	<	0.005	<	<	0.001	0.002	<	<	n.a.	n.a.	<	<	<	<	<	<
Nd	<	<	0.019	<	<	<	0.009	<	<	n.a.	n.a.	<	<	<	<	<	<
Sm	<	<	<	<	<	<	<	<	<	n.a.	n.a.	<	<	<	<	<	<
Eu	<	<	0.003	<	<	<	<	<	<	n.a.	n.a.	<	<	<	<	<	<
Gd	<	<	<	<	<	<	<	<	<	n.a.	n.a.	<	<	<	<	<	<
Tb	<	<	0.004	<	0.004	0.003	0.004	<	0.004	n.a.	n.a.	<	<	<	<	<	<
Dy	0.051	0.064	0.067	0.074	0.072	0.065	0.069	0.059	0.102	n.a.	n.a.	0.047	0.039	0.060	0.052	0.055	0.044
Ho	0.024	0.026	0.022	0.034	0.033	0.029	0.030	0.023	0.036	n.a.	n.a.	0.017	0.025	0.020	0.021	0.023	0.023

Er	0.11	0.14	0.12	0.13	0.15	0.15	0.14	0.13	0.20	n.a.	n.a.	0.10	0.14	0.10	0.12	0.12	0.09
Tm	0.019	0.026	0.021	0.032	0.030	0.030	0.027	0.026	0.039	n.a.	n.a.	0.023	0.031	0.022	0.022	0.018	0.019
Yb	0.21	0.21	0.20	0.22	0.26	0.25	0.25	0.23	0.37	n.a.	n.a.	0.20	0.24	0.18	0.20	0.20	0.17
Lu	0.031	0.036	0.036	0.039	0.047	0.039	0.041	0.037	0.062	n.a.	n.a.	0.036	0.042	0.031	0.029	0.035	0.031

Anal # = analytical point number, Mg# = Mg/(Mg+Fetotal) atomic ratio, Cr# = Cr/(Cr + AL) atomic ratio, LA dia = Laser diameter, < = lower than detection limit, n.a. = not analyzed

572

573

Table 4. Melting conditions and parameters used for geochemical models

Open system melting			**Mineral/melt partition coefficients**			
Starting compositions (1st stage melting)	5 % fractional melting from a DMM at garnet peridotite condition (see Fig. 8a)			Dol/lq	Dsp/lq	Dopx/lq
			La	0.000007	0.0008	0.0025
Influx melting (2nd stage melting)			Ce	0.00001	0.0008	0.005
degree of melting	13 % from residue after 1st melting at spinel peridotite condition		Sr	0.00019	0.0008	0.007
	Estimation of influx melting	Using influx composiitons of Li et al. (2013)	Nd	0.00007	0.0008	0.01
Result	Figure 8c	Figure 8d	Zr	0.007	0.07	0.07
critical melt fraction: α	0.05	0.02	Sm	0.0007	0.0008	0.02
dimensionless influx rate: β	1	0.02	Eu	0.00095	0.0008	0.03
Others	The effect of trapped melt crystallization was not considered.		Ti	0.015	0.15	0.15
			Dy	0.004	0.0015	0.05
Simplified plate model			Y	0.0065	0.00225	0.06
Starging compositions (see Fig. 8b)	5 % fractional melting at garnet peridotite then 13 % fractional melting at spinel peridotite		Er	0.009	0.003	0.07
percolating melt/fluid ratio	Gradual decreasing awasy from the starting point		Yb	0.009	0.0045	0.08
	clinopyroxene/melt mass ratio is changed from $\alpha 1 =1$, then $\alpha j= 2\,(j-1)$					
Result	Figures 8e and 8f					

574

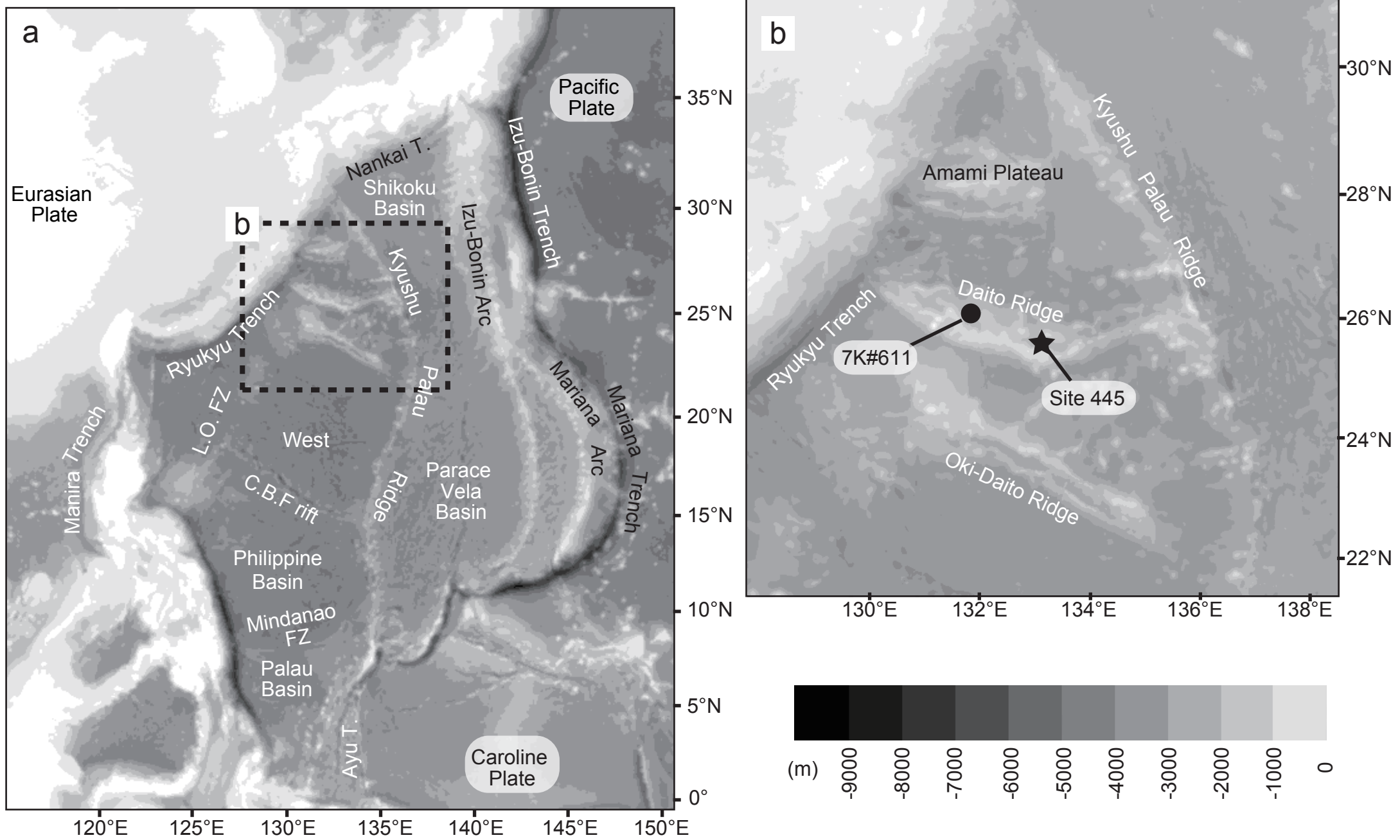**FIGURE 1. Morishita et al.**
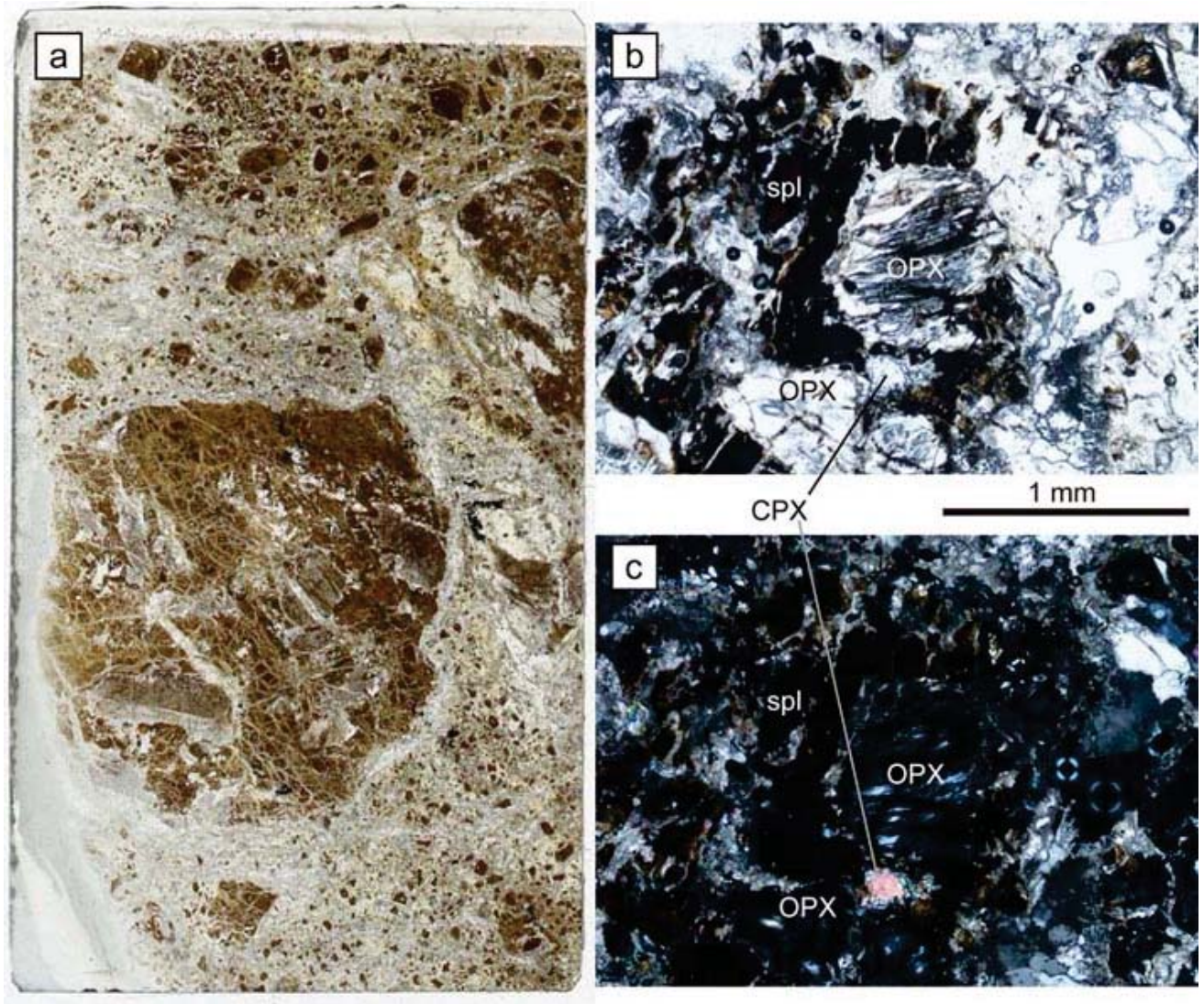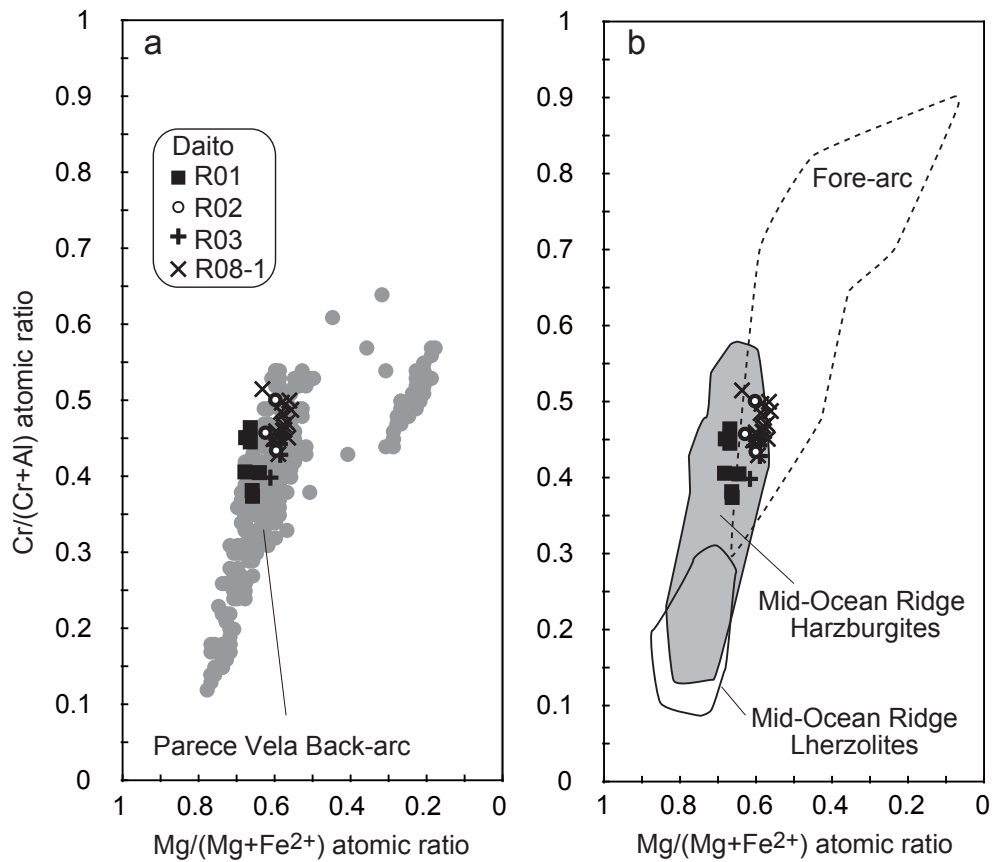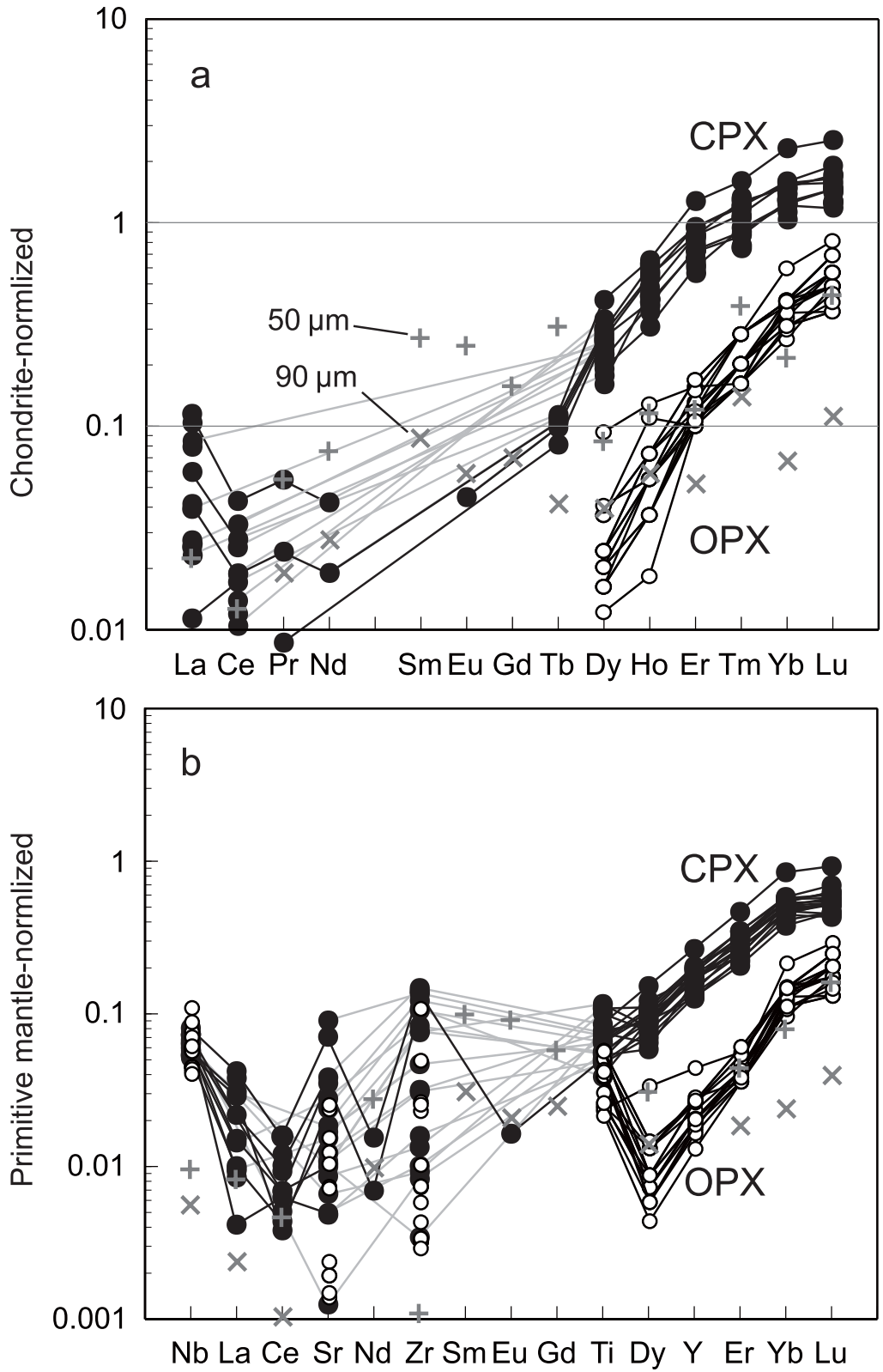
FIGURE 2. Morishita et al.
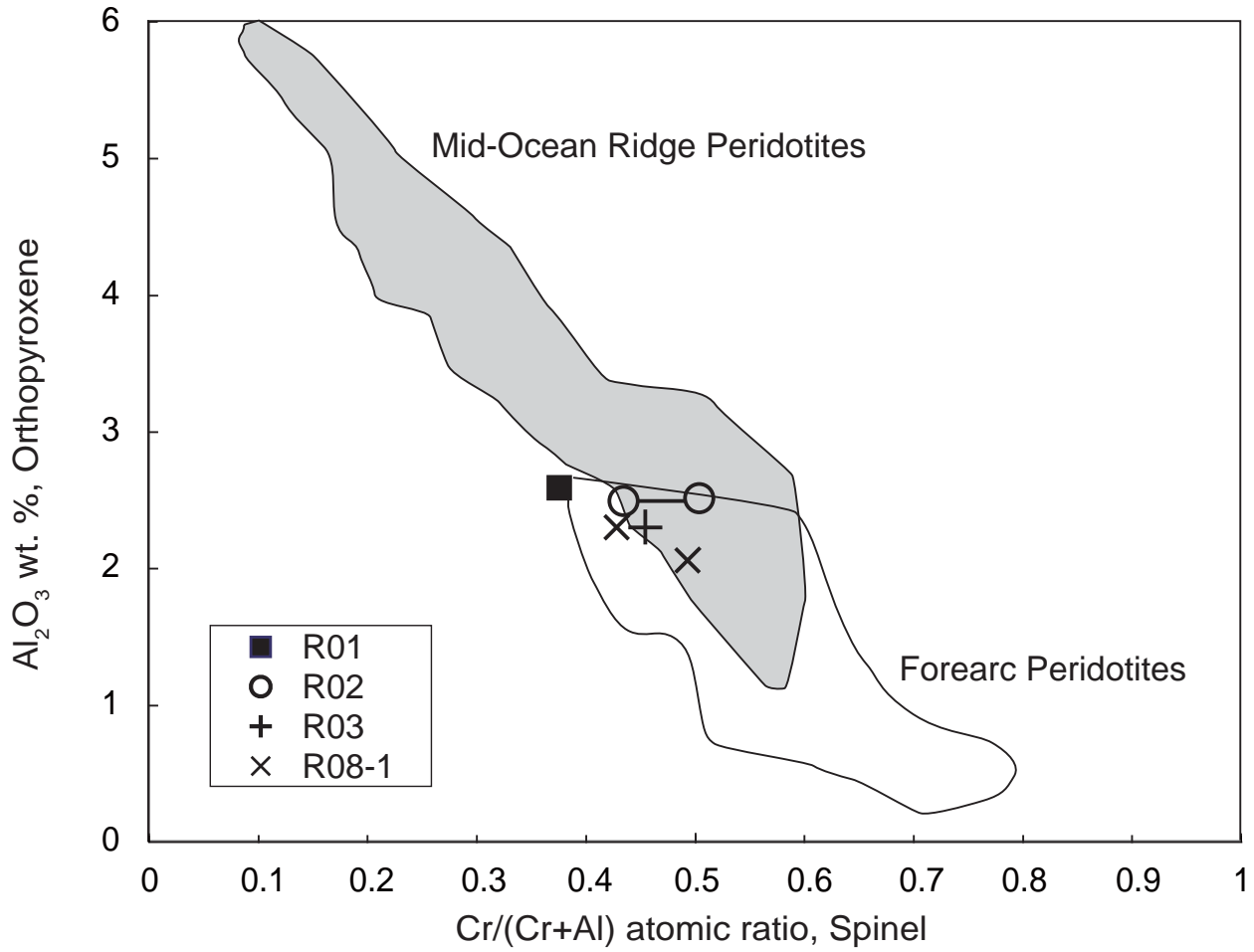
FIGURE 3. Morishita et al.

FIGURE 4. Morishita et al.

FIGURE 5. Morishita et al.

FIGURE 6. Morishita et al.

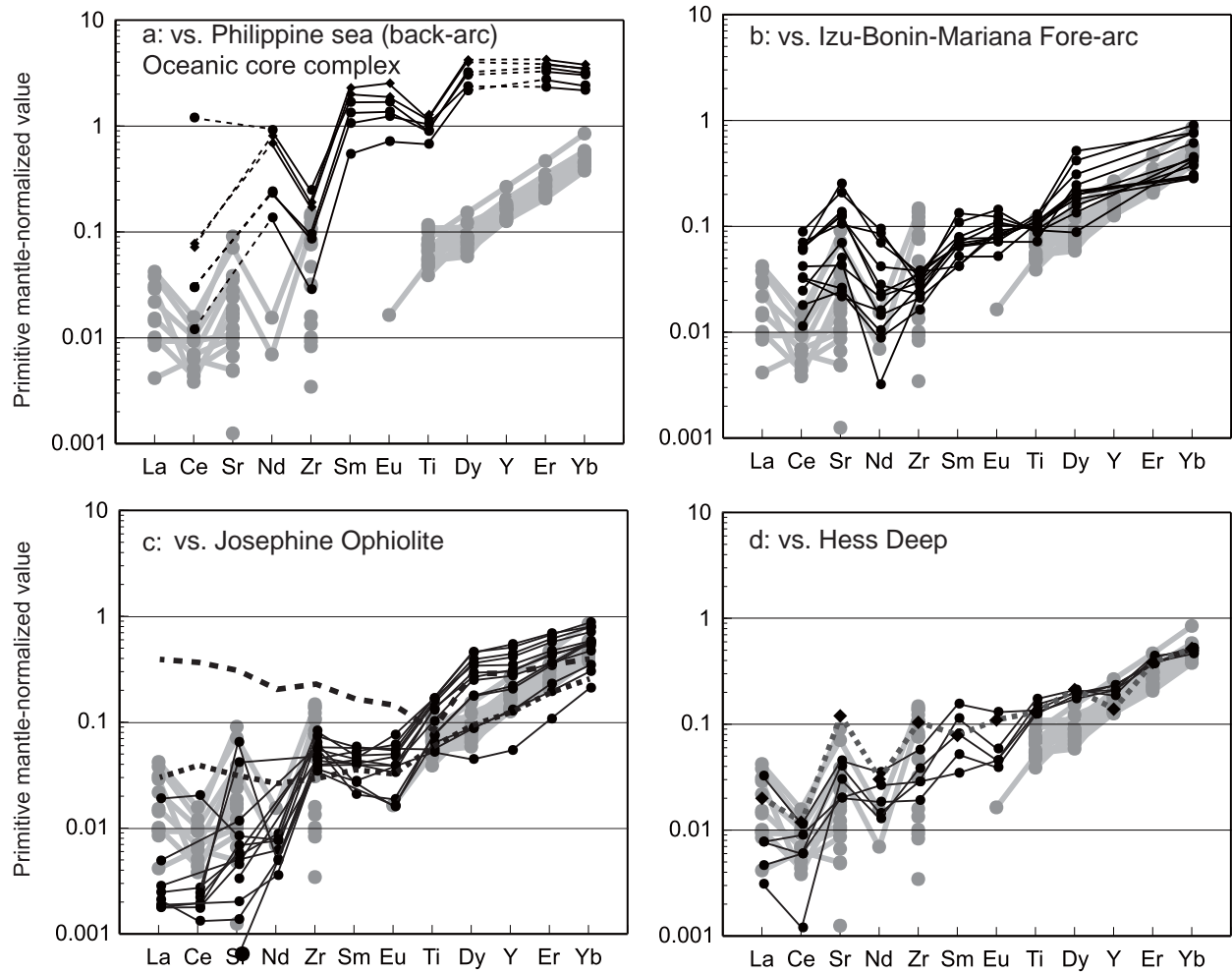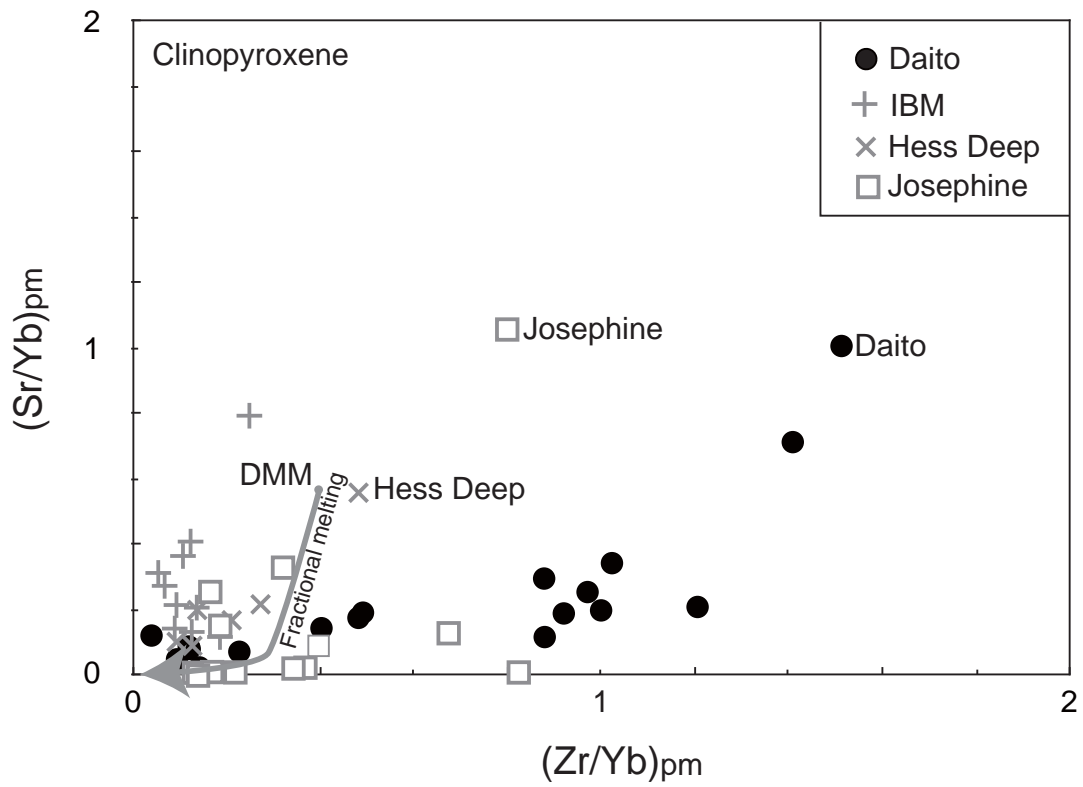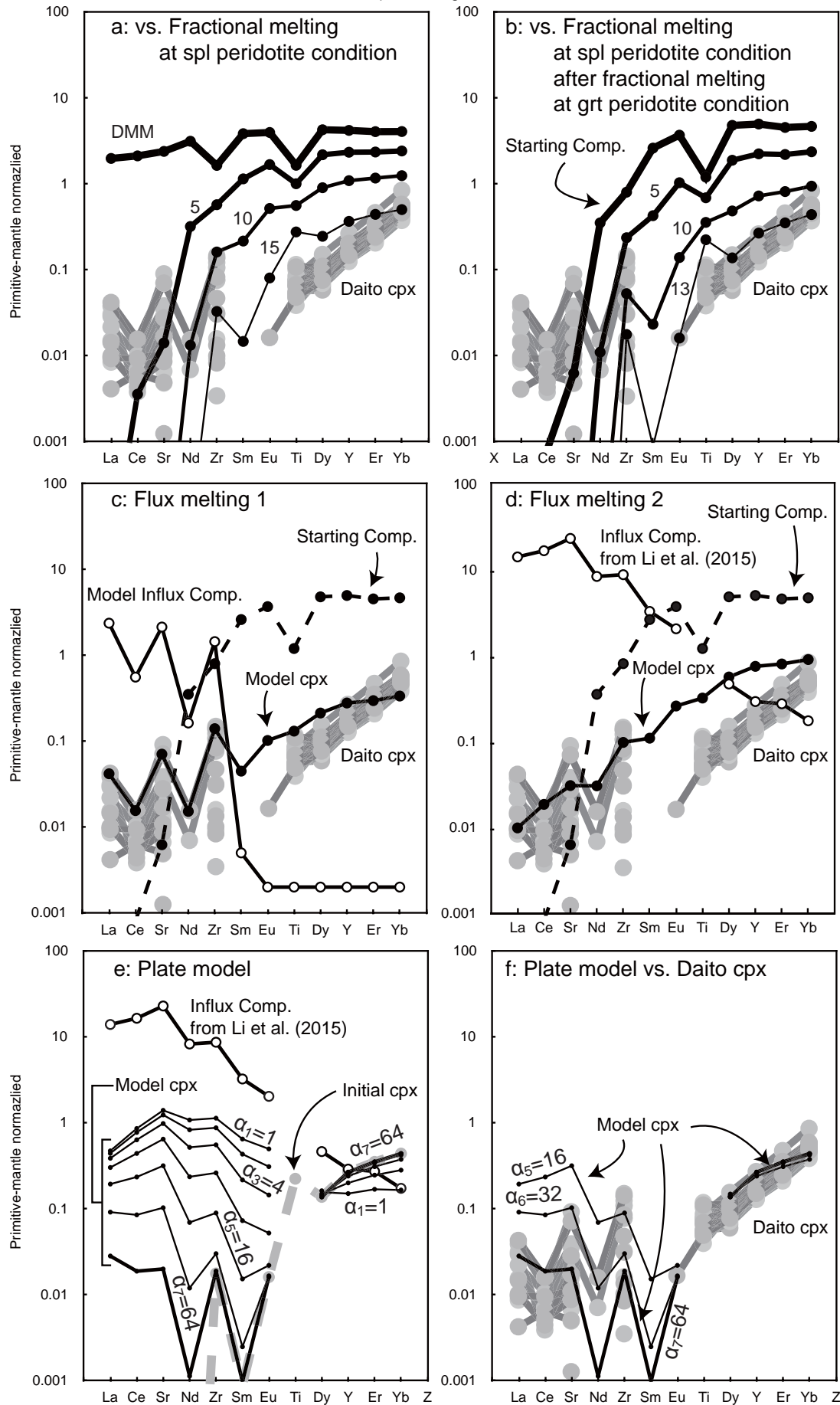**Figure 7. Morishita et al.**

FIGURE 8. Morishita et al.